ELSEVIER

Journal of Nuclear Materials 304 (2002) 63–72

journal of nuclear materials

www.elsevier.com/locate/jnucmat

Phase relations in the quaternary Fe–Pu–U–Zr system

Kinya Nakamura [a,*], Takanari Ogata [a], Masaki Kurata [a], Takeshi Yokoo [a], Michael A. Mignanelli [b]

[a] *Central Research Institute of Electric Power Industry, Pyro-process Fuel Cycle Project, Iwado-kita 2-11-1, Komae-shi, Tokyo 201-8511, Japan*

[b] *AEA Technology plc, 220 Harwell, Didcot, Oxfordshire OX11 0QJ, UK*

Received 27 November 2001; accepted 6 April 2002

Abstract

The phase diagram in the quaternary Fe–Pu–U–Zr system was established at 923 K in the uranium-rich region to understand better the compatibility between the metal fuel and stainless steel cladding in a fast reactor. The experimental phase relation data obtained in this study was applied to the thermodynamic methodology for construction of the phase diagram. The calculated phase diagram was consistent and well within the experimental data. The applicability of the thermodynamic model to other temperatures was confirmed by comparing the present results of differential thermal analysis with the calculated phase diagrams. These consistencies mean that both the thermodynamic model and the assessed parameters in the binary and ternary subsystems developed so far are reasonable. The calculated phase diagram established in this study was also in good agreement with the analysis of the diffusion zone in tests on Pu–U–Zr/Fe couples. This suggests that the diffusion zone formed at the fuel–cladding interface in the reactor system can be assessed using the phase diagram in the quaternary Fe–Pu–U–Zr system. © 2002 Published by Elsevier Science B.V.

PACS: 81.30.Bx; 64.70.Dv; 64.70.Kb

1. Introduction

Plutonium–uranium–zirconium (Pu–U–Zr) alloys have been considered one of the more promising advanced fuels in fast reactors because of good thermal response, enhanced reactor safety, ease of fabrication, and well suited to pyro-reprocessing. Compatibility of the Pu–U–Zr alloy fuel with the stainless steel cladding has been recognized as one of the major concerns for the fuel performance [1,2]. To achieve a better understanding of the compatibility, investigations of the diffusion zone structures at the fuel–cladding interface [3–6] and assessments of the related phase diagrams [7–11] have been performed.

The multi-component Fe–Pu–U–Zr quaternary system is one of the fundamental systems to simulate the fuel–cladding chemical interaction. In particular, the uranium-rich region in the quaternary system is important for the compatibility issue because the fuel composition is in the range $Pu_{0.1–0.2}U_{0.6–0.7}Zr_{0.2}$. An assessment of the ternary subsystems, Fe–Pu–U [7], Fe–U–Zr [8] and Pu–U–Zr [9], has been performed, and isothermal sections at 923 K for these ternary subsystems are represented in Fig. 1. Here, χ, ε and λ in the Fe–U–Zr system are ternary compounds having compositions of $Fe_{0.50}U_{0.18}Zr_{0.32}$, $Fe_{0.33}U_{0.17–0.34}Zr_{0.33–0.50}$ and $Fe_{0.06}U_{0.69–0.73}Zr_{0.21–0.25}$, respectively [8,10]. A solid solution of γU, εPu and βZr is designated as bcc in this paper. Kurata et al. [7] attempted to represent the quaternary phase diagram at 923 K based on assessment of the Gibbs energies for the binary and ternary subsystems, assuming that no plutonium dissolves in the χ, ε and λ phases, for example. Ogata et al. [5] examined the

* Corresponding author. Tel.: +81-3 3480 2111; fax: +81-3 3480 7956.

E-mail address: kinya@criepi.denken.or.jp (K. Nakamura).

0022-3115/02/$ - see front matter © 2002 Published by Elsevier Science B.V.
PII: S0022-3115(02)00855-3

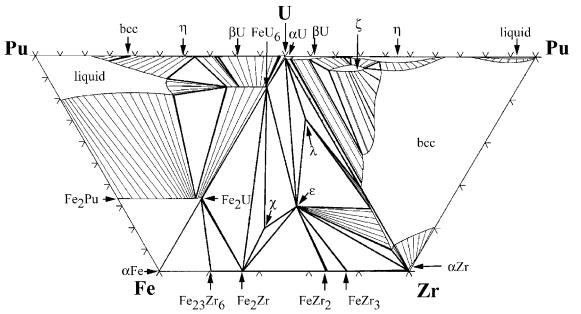

Fig. 1. Assessed isothermal sections at 923 K for the ternary Fe–Pu–U, Fe–U–Zr, and Pu–U–Zr systems quoted from Refs. [7–10].

reaction zones in the diffusion couples consisting of Pu–U–Zr alloys with Fe. The results of this examination provide qualitative information on the quaternary Fe–Pu–U–Zr phase relations.

This paper presents phase relation data in the uranium-rich region of the quaternary Fe–Pu–U–Zr system from annealing studies of the quaternary alloys at 923 K. Based on these experimental data, the quaternary phase diagram is established by applying the thermodynamic methodology used by Kurata et al. [7–9]. Predicted phase relations at other temperatures are compared with the results of differential thermal analysis (DTA) performed in this study to confirm the applicability of the diagram in other temperature regions. Finally, the diffusion test results in the Pu–U–Zr/Fe couples are analyzed by using the established quaternary phase diagram.

2. Experimental procedure

All experimental work was performed in glove boxes purged with pure argon gas. Six alloy compositions in the quaternary Fe–Pu–U–Zr system were selected from the multi-phase regions expected from the diffusion zone structure formed in the Pu–U–Zr/Fe couples [5]. The alloy ingots, designated as Q1 to Q6, were prepared from the pure metals by arc-melting on a water-cooled copper hearth. The purities of iron, uranium and zirconium were 99.995%, 99.9% and 99.9%, respectively. The plutonium metal contained ≈1.9 at.% of americium. The arc-melted alloy ingots were inverted and re-melted repeatedly to enhance their homogeneity. Ingot compositions based on the starting material weights are consistent with the results of the chemical analysis, as shown in Table 1. This confirms the homogeneity of the ingots. No analysis was performed for americium in this study.

2.1. Metallography

Samples were taken from the arc-melted alloy ingots, and their surfaces were filed to remove any potential oxide scale. Each sample was loaded in a lidded tungsten can, then encapsulated in a stainless steel container under an atmosphere of 0.1 MPa pure argon. The encapsulated samples were annealed at 923 K for 168 h or longer. After annealing, the samples were quenched in a silicone-oil bath and sectioned. The surfaces were prepared metallographically and then examined by electron probe microanalysis (EPMA). The composition of the observed phases were measured using an energy dispersive X-ray (EDX) detector. The intensities of FeK, PuLα, ULα and ZrK X-rays were converted to the atomic fractions by the ZAF correction.

2.2. Differential thermal analysis

Samples of ≈3 mm cube were taken from the arc-melted alloy ingots, Q1 to Q6. The surface of each sample was thoroughly filed to remove potential oxide scale. The sample was then placed into an aluminum oxide crucible positioned on the DTA sensor head. Loose-fitting tantalum lids were placed onto the crucible to reduce the oxidation of the reactive sample. During DTA operation, the inside of the DTA furnace was purged with highly purified argon gas flowing at 50 ml/min. Rates of heating and cooling were programmed at 10 and 20 K/min, respectively. The heating and cooling cycle was repeated in the temperature range of 773–1273

Table 1
Composition of quaternary Fe–Pu–U–Zr alloy samples

Alloy number	Composition fabricated (at.%)				Composition analyzed (at.%)						
	Fe	Pu	U	Zr	Fe	Pu	U	Zr	H[a]	O[a]	N[a]
Q1	43.1	10.0	26.4	20.4	42.2	10.4	28.0	19.4	23.5	211	<50
Q2	30.7	15.1	36.6	17.5	30.8	15.0	37.4	16.8	20.5	198	<50
Q3	47.5	13.2	28.9	10.4	47.6	12.9	29.5	10.0	12	178	<50
Q4	12.4	19.3	46.3	21.9	12.6	18.8	46.5	22.0	<10	31.5	<50
Q5	17.0	20.0	48.0	15.0	17.7	19.2	47.6	15.5	<10	72.5	<50
Q6	3.2	22.3	47.8	26.7	6.1	22.0	48.6	23.3	<10	63	<50

[a] wppm.

K to confirm reproducibility of the DTA curves. After the measurement, each sample could be easily removed from the crucible, where the surface of the sample in contact with the aluminum oxide remained shiny. The phase transition temperatures were determined from the DTA curves on heating. The temperature calibration was accomplished regularly by measuring the melting point of high purity metals of aluminum, silver and zinc.

3. Quaternary phase diagram at 923 K

3.1. Experimental phase relations

Typical back-scattered electron (BSE) images of the quenched alloy samples are shown in Fig. 2. Since no quaternary compounds were observed in the composition region examined in this study, the observed phases

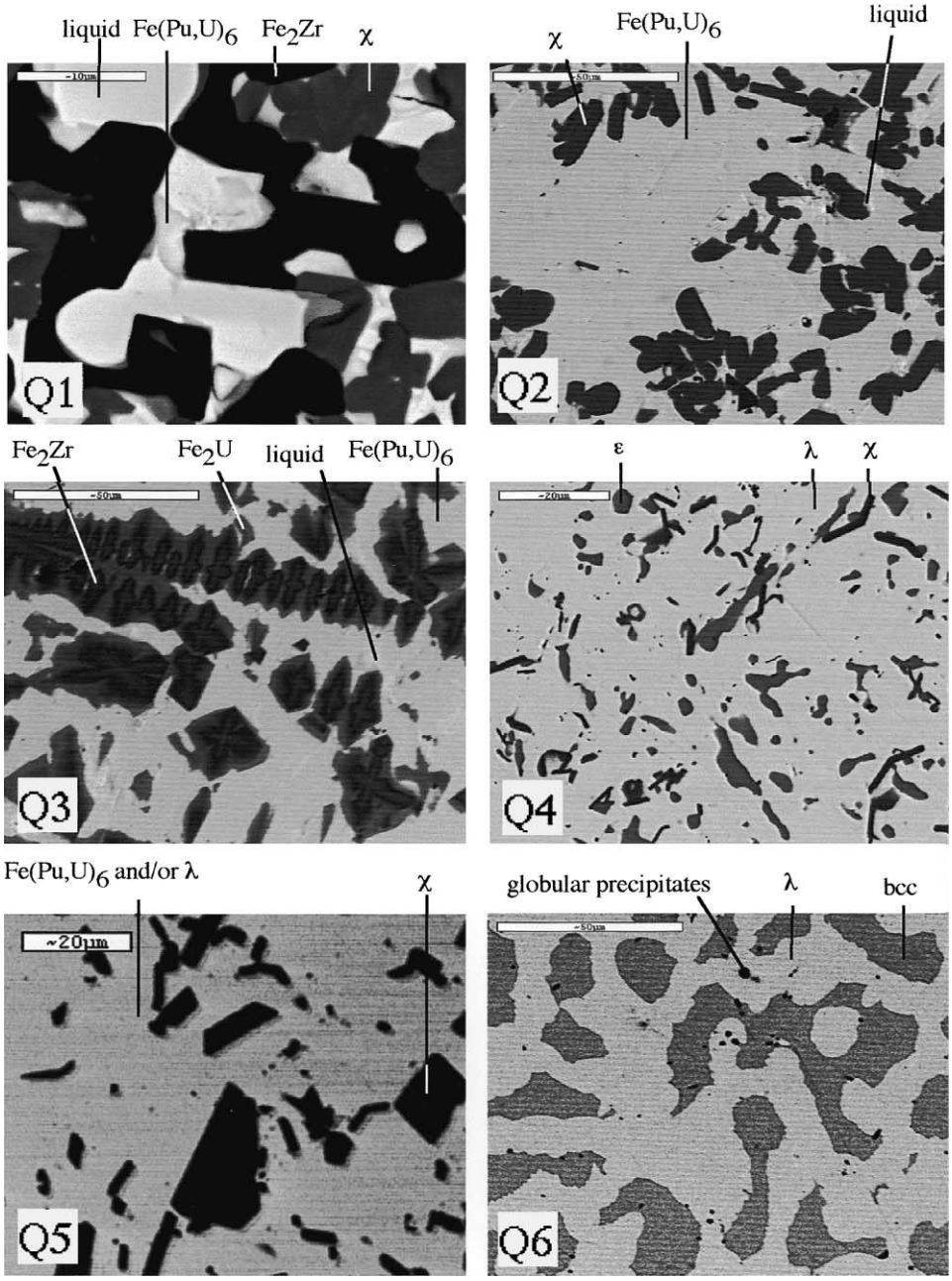

Fig. 2. Back-scattered electron images of the quaternary alloy samples annealed at 923 K.

could be identified based on the ternary subsystems Fe–Pu–U, Fe–U–Zr, and Pu–U–Zr. The composition analysis results are summarized in Table 2 together with the identified phases.

In the case of sample Q5, only two regions, light and dark, are seen in the BSE image (Fig. 2), but X-ray mapping images shown in Fig. 3 indicate that the light region in the BSE image consists of two different phases. They correspond to phases with a high-U and low-Pu concentration and low-U and high-Pu concentration. From the EDX results, the mole ratio of Fe:(Pu + U + Zr) in the former phase is ≈1:6 and the ratio of Fe:(Pu + U):Zr in the latter phase is ≈6:71:23. It was then concluded that the former is the Fe(Pu, U)$_6$ phase, and the latter the λ phase dissolving about 32 at.% Pu in the uranium sites. The plutonium-rich phases are also observed in samples Q1 to Q3. The compositions were nonhomogeneous and have an average of 70 at.% Pu or more. From the ternary Fe–Pu–U system (see Fig. 1), it is suggested that the plutonium-rich phase segregated from the liquid at 923 K during cooling and solidification. Globular precipitates about a few microns in diameter are observed in the quenched alloy sample Q6 as shown in Fig. 2. These precipitates are assumed to be αZr stabilized by oxygen [12] because the results of the EPMA showed excess amounts of zirconium and oxygen in these precipitates.

The experimental phase relations in the quaternary Fe–Pu–U–Zr system at 923 K are represented in Fig. 4 and are based on the results shown in Table 2, which are a part of the compositional tetrahedron. The bottom surface corresponds to the ternary Fe–U–Zr, the left-back side to the Fe–Pu–U, and the right-back side to the Pu–U–Zr subsystems. The following information on the phase relations at 923 K can be derived from Fig. 4 and Table 2: (1) liquid phase is in equilibrium with the Fe(Pu, U)$_6$, Fe$_2$U, Fe$_2$Zr, and χ phases, (2) solubility of Zr in the Fe(Pu, U)$_6$ phase is small (about 4 at.%), (3) solubility of Pu in the Fe$_2$Zr and χ phases are also small (≈3 and 2 at.%, respectively), (4) solubility of Pu in the uranium sites of the λ phase is rather large (32 at.% or more), and (5) the λ phase is in equilibrium with the Fe(Pu, U)$_6$ and χ phases, which is not the case in the ternary Fe–U–Zr subsystem [8,10].

3.2. Construction of quaternary phase diagram

Kurata et al. [7] estimated the phase diagram in the quaternary Fe–Pu–U–Zr system based on the assessed Gibbs energies for the binary and ternary subsystems. In the calculation, the solubility of Zr in Fe(Pu, U)$_6$ and of Pu in Fe$_2$Zr, χ, ε and λ phases were assumed to be negligible. The present results of the composition analysis suggest that the above assumptions are reasonable

Table 2
EDX analysis results of the quaternary alloy samples annealed at 923 K

Alloy number	Composition (at.%)				Identified phases
	Fe	Pu	U	Zr	
Q1	13.5	15.8	66.3	4.4	Fe(Pu, U)$_6$
	50.5	1.6	18.7	29.3	χ
	67.2	0.8	3.4	28.7	Fe$_2$Zr
	10.6	73.9	8.1	7.4	(plutonium-rich)[a]
Q2	13.2	16.8	66.9	3.1	Fe(Pu, U)$_6$
	50.3	1.0	17.8	31.0	χ
	5.7	81.1	7.2	6.0	(plutonium-rich)[a]
Q3	13.0	20.1	62.9	4.0	Fe(Pu, U)$_6$
	64.7	3.0	23.3	9.0	Fe$_2$U
	65.2	3.0	13.2	18.6	Fe$_2$Zr
	10.3	76.5	9.3	3.9	(plutonium-rich)[a]
Q4	5.0	25.2	50.6	19.2	λ
	30.2	4.6	26.9	38.3	ε
	48.0	1.8	18.9	31.3	χ
Q5	12.9	16.1	67.8	3.3	Fe(Pu, U)$_6$
	5.5	32.7	48.9	12.9	λ
	50.9	0.8	18.0	30.3	χ
Q6	5.6	25.1	48.1	21.2	λ
	0.2	26.4	36.7	36.7	bcc

[a] Concentration of Pu up to 90 at.% were measured in the plutonium-rich region.

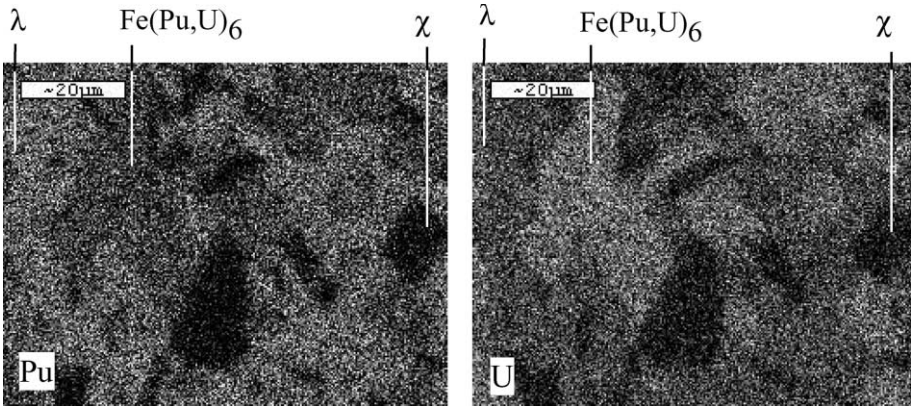

Fig. 3. X-ray mapping images of the alloy sample Q5 in Fig. 2.

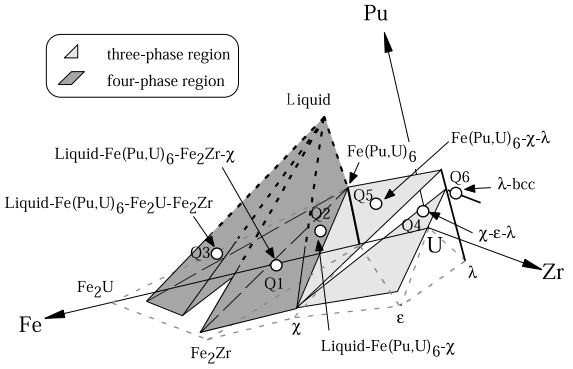

Fig. 4. Experimental phase relations in the quaternary Fe–Pu–U–Zr system at 923 K.

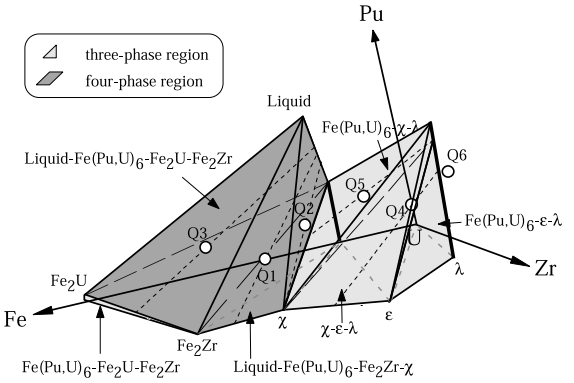

Fig. 5. Calculated phase diagram in the quaternary Fe–Pu–U–Zr system at 923 K.

except for the solubility of Pu in the λ phase. Hence, the thermodynamic methodology used by Kurata et al. [7] was applied to the construction of the quaternary phase diagram by introducing the model that plutonium can substitute for uranium in the uranium-sites of the λ phase. The λ phase was modeled using a three-sublattice model $Fe_a(Pu, U)_bZr_c$, with the Gibbs energy of mixing of the λ phase given by

$$G^{\lambda}_{\mathrm{mix}} = y_{\mathrm{Pu}}\,{}^{0}G^{\lambda}_{\mathrm{Fe:Pu:Zr}} + y_{\mathrm{U}}\,{}^{0}G^{\lambda}_{\mathrm{Fe:U:Zr}} + bRT(y_{\mathrm{Pu}}\ln y_{\mathrm{Pu}} + y_{\mathrm{U}}\ln y_{\mathrm{U}}) + y_{\mathrm{Pu}}y_{\mathrm{U}}L^{\lambda}_{\mathrm{Fe:Pu,U:Zr}}.$$

Here, the sublattice fractions denoted a, b and c are set to be 0.06, 0.71 and 0.23, respectively, based on the literature [8,10]. The variable y_i represents the site fraction of component i in the second sublattice ($\Sigma y_i = 1$), ${}^{0}G^{\lambda}_{\mathrm{Fe:Pu:Zr}}$ and ${}^{0}G^{\lambda}_{\mathrm{Fe:U:Zr}}$ the Gibbs energy of formation of the λ phase in the ternary Fe–Pu–Zr and Fe–U–Zr systems, respectively, and $L^{\lambda}_{\mathrm{Fe:Pu,U:Zr}}$ the interaction parameter between plutonium and uranium in the second sublattice. Both values of ${}^{0}G^{\lambda}_{\mathrm{Fe:Pu:Zr}}$ and $L^{\lambda}_{\mathrm{Fe:Pu,U:Zr}}$, which have to be evaluated to assess the quaternary phase diagram, cannot be assessed simultaneously due to insufficient thermodynamic data and phase diagram information. If the contribution of the parameter $L^{\lambda}_{\mathrm{Fe:Pu,U:Zr}}$ can be considered to be included completely in the ${}^{0}G^{\lambda}_{\mathrm{Fe:Pu,U:Zr}}$ term (namely $L^{\lambda}_{\mathrm{Fe:Pu,U:Zr}}$ assumes to be zero), deviation of the Gibbs energy of mixing becomes large in the plutonium-rich region but relatively small in the uranium-rich region. From a standpoint of the aim of this study (construction of the uranium-rich region of the quaternary phase diagram), we could consider it reasonable to neglect the interaction in the second sublattice. Based on the above consideration, the assessment of the quaternary phase diagram at 923 K was performed. When the value of ${}^{0}G^{\lambda}_{\mathrm{Fe:Pu:Zr}}$ is -12.2 to -13.4 kJ/g-atom, the experimental phase relation observed in the Q5 sample, three-phase equilibrium Fe(Pu, U)$_6$–χ–λ, can be reproduced. Here, the reference states of the pure solid elements at 298.15 K are bcc-Fe, monoclinic-Pu, orthorhombic-U, and hcp-Zr.

The calculated phase diagram in the uranium-rich region of the quaternary system at 923 K is shown in

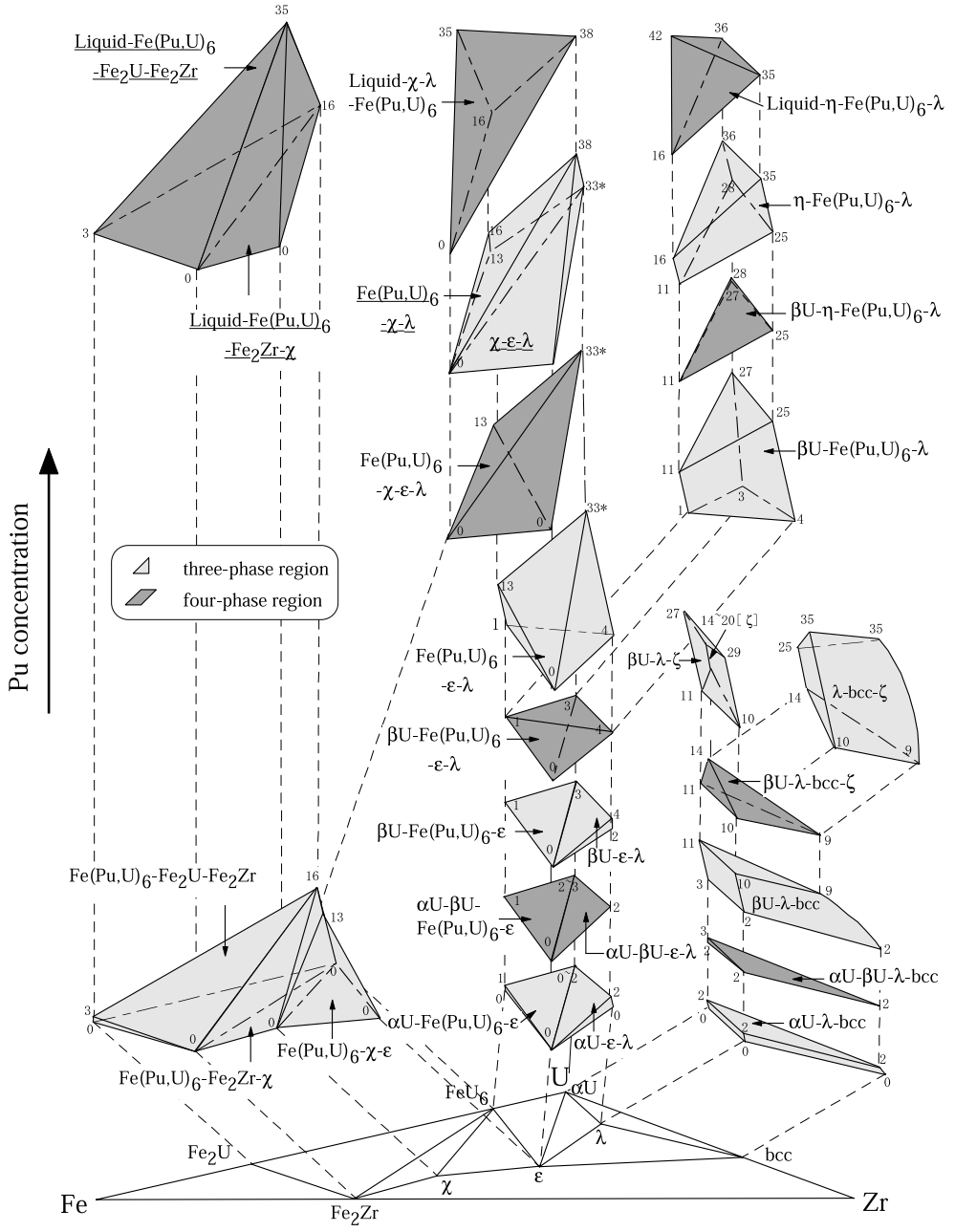

* Experimental phase relation data show the change of tieline from $Fe(Pu,U)_6$-ε to λ-χ below 25 at.% of Pu in the λ-phase.

Fig. 6. Schematic description of the calculated phase diagram in the quaternary Fe–Pu–U–Zr system at 923 K. Only three-phase and four-phase regions are shown in order of Pu concentration. Numbers noted in the figure mean the concentration of Pu in each phase. The experimental phase regions observed in this study are underlined.

Fig. 5. Here, the value of ${}^0G^{\lambda}_{Fe:Pu:Zr}$ is set to be −13.0 kJ/g-atom. The calculated phase diagram agrees with the experimental phase relations observed in this study. This agreement suggests that the assumption above is reasonable at least in the uranium-rich region and the thermodynamic assessment of each subsystem is excellent.

To better understand the description of the quaternary phase relations, the quaternary phase diagram is shown schematically in Fig. 6. Here, only three-phase

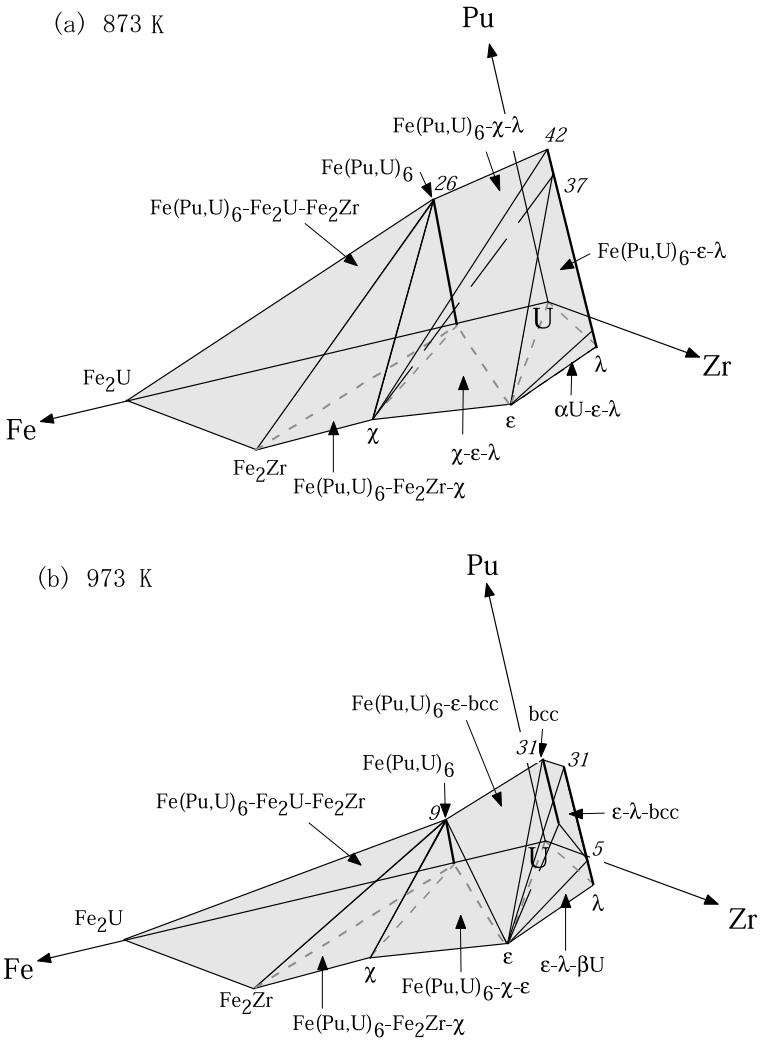

Fig. 7. Calculated phase diagrams in the quaternary Fe–Pu–U–Zr system at (a) 873 K and (b) 973 K. Numbers noted in the figure refer to the concentration of Pu in each phase.

and four-phase regions are shown in light and dark gray, respectively, as tetrahedrons. The multi-phase regions observed in this study are underlined in Fig. 6. Numbers noted in the figure show the calculated concentration of Pu in each phase in the three-phase regions.

4. Quaternary phase diagram at other temperatures

The thermodynamic methodology described in the previous chapter was used to predict the quaternary phase diagrams at different temperatures. For example, Fig. 7 shows the calculated phase diagrams at 873 and 973 K, showing a part of the solid phase regions. It is predicted that there is no change in the phase relations at 873 K qualitatively compared with those at 923 K, although the λ phase is not in equilibrium with the Fe(Pu, U)$_6$ phase at 973 K while it is at 873 and 923 K.

Phase transition reactions and corresponding phase transition temperatures for the alloy compositions Q1 to Q6 were predicted from the calculated phase diagrams. The predicted phase transition reactions were compared with the thermal events observed in the DTA curves, then phase transition temperatures were read from the DTA curves based on the comparison results. Since gradual endothermic transition reactions do not necessarily show significant deviations from the baseline on the DTA curves, several phase transition temperatures could not be determined from the DTA tests. The phase transition temperatures between the calculated phase

Table 3
Comparison of the phase transition temperatures for the quaternary alloy compositions between the calculated phase diagram and the DTA results

Alloy number	Phase transition temperature (K)		Phase transition reactions
	Calculated	DTA	
Q1	844	ND	$\chi + Fe(Pu, U)_6 + Fe_2Zr + \lambda \rightarrow Fe(Pu, U)_6 + Fe_2Zr + \lambda$
	904	874	$Fe(Pu, U)_6 + Fe_2Zr + \lambda \rightarrow Liquid + Fe(Pu, U)_6 + Fe_2Zr + \lambda$
	914	908	$Liquid + Fe(Pu, U)_6 + Fe_2Zr + \lambda \rightarrow Liquid + Fe(Pu, U)_6 + Fe_2Zr$
	915	928	$Liquid + Fe(Pu, U)_6 + Fe_2Zr \rightarrow Liquid + Fe(Pu, U)_6 + Fe_2Zr + \chi$
	962	953	$Liquid + Fe(Pu, U)_6 + Fe_2Zr + \chi \rightarrow Liquid + Fe_2Zr + \chi$
	1091	1033	$Liquid + Fe_2Zr + \chi \rightarrow Liquid + Fe_2Zr + \chi + \varepsilon$
	1094	ND	$Liquid + Fe_2Zr + \chi + \varepsilon \rightarrow Liquid + Fe_2Zr + \varepsilon$
	1115	ND	$Liquid + Fe_2Zr + \varepsilon \rightarrow Liquid + Fe_2Zr$
Q2	915	ND	$Fe(Pu, U)_6 + Fe_2Zr + \chi + \lambda \rightarrow Fe(Pu, U)_6 + \chi + \lambda$
	915	ND	$Fe(Pu, U)_6 + \chi + \lambda \rightarrow Liquid + Fe(Pu, U)_6 + \chi + \lambda$
	942	ND	$Liquid + Fe(Pu, U)_6 + \chi + \lambda \rightarrow Liquid + Fe(Pu, U)_6 + \chi$
	942	968	$Liquid + Fe(Pu, U)_6 + \chi \rightarrow Liquid + Fe(Pu, U)_6 + \chi + \varepsilon$
	957	ND	$Liquid + Fe(Pu, U)_6 + \chi + \varepsilon \rightarrow Liquid + \chi + \varepsilon$
	1068	ND	$Liquid + \chi + \varepsilon \rightarrow Liquid + Fe_2Zr + \chi + \varepsilon$
	1078	1075	$Liquid + Fe_2Zr + \chi + \varepsilon \rightarrow Liquid + Fe_2Zr + \varepsilon$
	1142	1153	$Liquid + Fe_2Zr + \varepsilon \rightarrow Liquid + Fe_2Zr$
	1247	ND	$Liquid + Fe_2Zr \rightarrow Liquid$
Q3	849	823	$Fe(Pu, U)_6 + Fe_2U + Fe_2Zr \rightarrow Liquid + Fe(Pu, U)_6 + Fe_2U + Fe_2Zr$
	934	923	$Liquid + Fe(Pu, U)_6 + Fe_2U + Fe_2Zr \rightarrow Liquid + Fe_2U + Fe_2Zr$
	1268	ND	$Liquid + Fe_2U + Fe_2Zr \rightarrow Liquid + Fe_2Zr$
Q4[a]	–	ND	$\chi + \varepsilon + \lambda + Fe(Pu, U)_6 \rightarrow \chi + \varepsilon + \lambda$
	–	944	$\chi + \varepsilon + \lambda \rightarrow \chi + \varepsilon + \lambda + Fe_2Zr$
	–	975	$\chi + \varepsilon + \lambda + Fe_2Zr \rightarrow \varepsilon + \lambda + Fe_2Zr$
	–	1008	$\varepsilon + \lambda + Fe_2Zr \rightarrow Liquid + \varepsilon + \lambda + Fe_2Zr$
	–	ND	$Liquid + \varepsilon + \lambda + Fe_2Zr \rightarrow Liquid + \varepsilon + \lambda$
	–	1034	$Liquid + \varepsilon + \lambda \rightarrow Liquid + \varepsilon + bcc$[b]
	–	ND	$Liquid + \varepsilon + bcc \rightarrow Liquid + bcc$
Q5	933	ND	$Fe(Pu, U)_6 + \chi + \varepsilon + \lambda \rightarrow Fe(Pu, U)_6 + \chi + \lambda$
	940	945	$Fe(Pu, U)_6 + \chi + \lambda \rightarrow Liquid + Fe(Pu, U)_6 + \chi + \lambda$
	940	ND	$Liquid + Fe(Pu, U)_6 + \chi + \lambda \rightarrow Liquid + Fe(Pu, U)_6 + \lambda$
	940	ND	$Liquid + Fe(Pu, U)_6 + \lambda \rightarrow Liquid + Fe(Pu, U)_6 + \varepsilon + \lambda$
	961	968	$Liquid + Fe(Pu, U)_6 + \varepsilon + \lambda \rightarrow Liquid + \varepsilon + \lambda$
	961	ND	$Liquid + \varepsilon + \lambda \rightarrow Liquid + \varepsilon + \lambda + bcc$
	1007	999	$Liquid + \varepsilon + \lambda + bcc \rightarrow Liquid + \varepsilon + bcc$[b]
	1053	ND	$Liquid + \varepsilon + bcc \rightarrow Liquid + \varepsilon$
	1247	ND	$Liquid + \varepsilon \rightarrow Liquid$
Q6	860	825	$\lambda + \delta + \zeta \rightarrow \lambda + \delta + bcc + \zeta$
	861	845	$\lambda + \delta + bcc + \zeta \rightarrow \lambda + bcc + \zeta$
	922	923	$\lambda + bcc + \zeta \rightarrow \lambda + bcc$
	1024	ND	$\lambda + bcc \rightarrow \lambda + \varepsilon + bcc$
	1034	1007	$\lambda + \varepsilon + bcc \rightarrow \varepsilon + bcc$[b]
	1071	ND	$\varepsilon + bcc \rightarrow Liquid + \varepsilon + bcc$
	1072	1118	$Liquid + \varepsilon + bcc \rightarrow Liquid + bcc$

ND: not determined because of gradual phase transition reaction on the DTA curves.

[a] In the case of the alloy composition Q4, the phase transition reactions predicted from the calculated phase diagram were inconsistent with DTA curve. The reason for the disagreement is thought that the calculated tie-lines in the vicinity of the composition deviate slightly from the experimental ones and show different phase equilibrium.

[b] The λ phase peritectoidally decomposes to two phases ε and bcc in the Fe–U–Zr ternary system [8].

diagrams and the DTA results agree with each other except for the alloy composition Q4, as shown in Table 3. The agreement suggests that the calculated phase diagrams are applicable to other temperatures.

5. Application of quaternary phase diagram to diffusion zone analysis

The application of the quaternary phase diagram to the analysis of the diffusion zone between the metal fuel and the cladding is discussed in this section. Ogata et al. [5] examined the reaction zones in two kinds of the diffusion couples consisting of Pu–U–Zr alloys with Fe annealed at 923 K. In Fig. 8, the average compositional changes in the diffusion zones, which are called 'schematic diffusion paths' in the literature [5], are plotted schematically in the calculated phase diagram at 923 K established in this study. Consecutive changes in composition can be seen in the diffusion zones, except for the interfaces between the region (e)–(f) in Fig. 8(i) and region (m)–(n) in Fig. 8(ii) drawn as dash-dotted lines. In these exceptional regions, it is not obvious from the EPMA whether the average compositional changes are consecutive or not.

Fig. 8 shows that there is good agreement between the calculated phase diagram and the results of the diffusion zone analysis. The calculations can be used to explain the different diffusion layers between the two couples, for example that the ε phase was formed only in the $Pu_{0.13}U_{0.65}Zr_{0.22}$/Fe couple. The reasonable correspondence suggests that the diffusion layers formed at

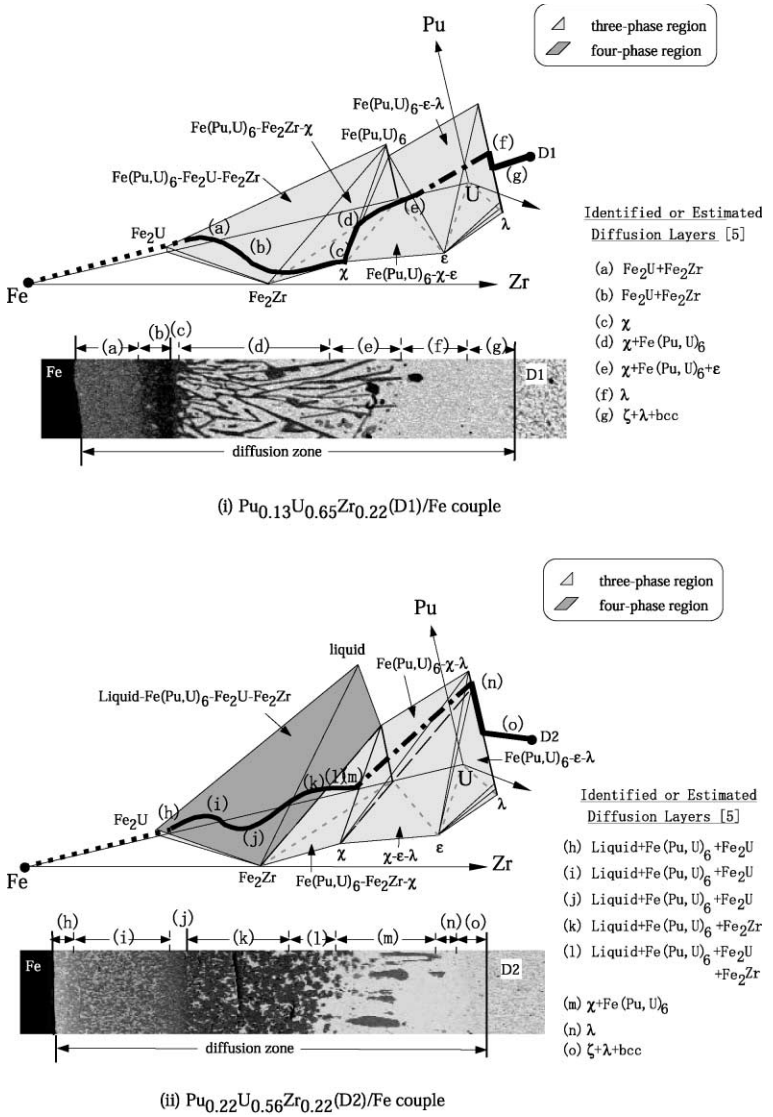

Fig. 8. Comparison of the calculated phase diagram in the quaternary Fe–Pu–U–Zr system at 923 K with the schematic diffusion paths observed in the Pu–U–Zr/Fe couples annealed at 923 K [5].

the metal fuel-stainless steel cladding interface can be analyzed with the phase diagram for the quaternary Fe–Pu–U–Zr system established in this study.

6. Conclusions

Phase relation data in the quaternary Fe–Pu–U–Zr system were obtained by annealing six compositions of the quaternary alloys at 923 K. The following information could be derived from the experimental results.

(1) liquid phase is in equilibrium with the $Fe(Pu, U)_6$, Fe_2U, Fe_2Zr and χ phases,
(2) solubility of Zr in the $Fe(Pu, U)_6$ phase is about 4 at.%,
(3) solubility of Pu in the Fe_2Zr and χ phases are $\approx$3 and 2 at.%, respectively,
(4) solubility of Pu in the uranium site of the λ phase is at least 32 at.%, and
(5) the λ phase is in equilibrium with the $Fe(Pu, U)_6$ and χ phases.

The phase diagram in the quaternary Fe–Pu–U–Zr system was established at 923 K in the uranium-rich region by applying the thermodynamic methodology used by Kurata et al., to the experimental data. The calculated phase diagram agreed with the experimental phase relations. The applicability of the calculated phase diagram to other temperatures was confirmed from an assessment of DTA results. The calculated phase diagram established in this study was also in good agreement with the experimental results from the analysis of the diffusion zone in Pu–U–Zr/Fe couples.

Acknowledgements

We thank Messrs J.J.W. Green, A.J. Jeffery, and Dr I.A. Vatter, AEA Technology plc., for their experimental support.

References

[1] T. Ogata, PhD thesis, Kyoto University, Kyoto, 2000.
[2] A.B. Cohen, H. Tsai, L.A. Neimark, J. Nucl. Mater. 204 (1993) 244.
[3] T. Ogata, M. Kurata, K. Nakamura, A. Itoh, M. Akabori, J. Nucl. Mater. 250 (1997) 171.
[4] K. Nakamura, T. Ogata, M. Kurata, A. Itoh, M. Akabori, J. Nucl. Mater. 275 (1999) 246.
[5] T. Ogata, K. Nakamura, M. Kurata, T. Yokoo, M.A. Mignanelli, J. Nucl. Sci. Technol. 37 (2000) 244.
[6] K. Nakamura, T. Ogata, M. Kurata, T. Yokoo, M.A. Mignanelli, J. Nucl. Sci. Technol. 38 (2001) 112.
[7] M. Kurata, K. Nakamura, T. Ogata, J. Nucl. Mater. 294 (2001) 123.
[8] M. Kurata, T. Ogata, K. Nakamura, T. Ogawa, J. Alloys Comp. 271&273 (1998) 636.
[9] M. Kurata, Calphad 23 (2000) 305.
[10] K. Nakamura, M. Kurata, T. Ogata, A. Itoh, M. Akabori, J. Nucl. Mater. 275 (1999) 151.
[11] K. Nakamura, M. Kurata, T. Ogata, T. Yokoo, M.A. Mignanelli, J. Phase Equilibria 22 (2001) 259.
[12] L. Leibowitz, E. Veleckis, R.A. Blomquist, J. Nucl. Mater. 154 (1988) 145.